



Quantitative imaging of water, ice and air in permafrost systems through petrophysical joint inversion of seismic refraction and electrical resistivity data

F.M. Wagner¹, C. Mollaret², T. Günther³, A. Kemna¹ and C. Hauck²

¹Institute of Geosciences, Geophysics Section, University of Bonn, Bonn, Germany. E-mail: mail@fwagner.info

²Department of Geosciences, University of Fribourg, Fribourg, Switzerland

³Leibniz Institute for Applied Geophysics, Hannover, Germany

Accepted 2019 August 31. Received 2019 June 17; in original form 2019 August 13

SUMMARY

Quantitative estimation of pore fractions filled with liquid water, ice and air is crucial for a process-based understanding of permafrost and its hazard potential upon climate-induced degradation. Geophysical methods offer opportunities to image distributions of permafrost constituents in a non-invasive manner. We present a method to jointly estimate the volumetric fractions of liquid water, ice, air and the rock matrix from seismic refraction and electrical resistivity data. Existing approaches rely on conventional inversions of both data sets and a suitable *a priori* estimate of the porosity distribution to transform velocity and resistivity models into estimates for the four-phase system, often leading to non-physical results. Based on two synthetic experiments and a field data set from an Alpine permafrost site (Schilthorn, Bernese Alps and Switzerland), it is demonstrated that the developed petrophysical joint inversion provides physically plausible solutions, even in the absence of prior porosity estimates. An assessment of the model covariance matrix for the coupled inverse problem reveals remaining petrophysical ambiguities, in particular between ice and rock matrix. Incorporation of petrophysical *a priori* information is demonstrated by penalizing ice occurrence within the first two meters of the subsurface where the measured borehole temperatures are positive. Joint inversion of the field data set reveals a shallow air-rich layer with high porosity on top of a lower-porosity subsurface with laterally varying ice and liquid water contents. Non-physical values (e.g. negative saturations) do not occur and estimated ice saturations of 0–50 per cent as well as liquid water saturations of 15–75 per cent are in agreement with the relatively warm borehole temperatures between -0.5 and 3 °C. The presented method helps to improve quantification of water, ice and air from geophysical observations.

Key words: Hydrogeophysics; Electrical resistivity tomography (ERT); Inverse theory; Joint inversion; Seismic tomography.

1 INTRODUCTION

Climate-induced degradation of permafrost can release substantial amounts of soil organic carbon into the atmosphere (e.g. Schuur *et al.* 2015) and increase the probability of slope failures in Alpine regions (e.g. Huggel *et al.* 2012). Understanding hydrological processes in permafrost systems is crucial to parametrize numerical models that simulate the evolution and potential carbon feedback of terrestrial permafrost as well as to assess the hazard potential of permafrost degradation on a physical basis.

While borehole information is expensive and limited to discrete locations, geophysical imaging offers opportunities to derive quantitative and non-invasive insights on permafrost characteristics at high

spatial and temporal resolution. Electrical resistivity and acoustic velocity of a medium are sensitive to the phase change of water between its liquid, frozen, and gaseous states. Electrical resistivity tomography (ERT) and refraction seismic tomography (RST) are thus widely used in cryospheric geophysical applications (Hauck & Kneisel 2008).

Hilbich *et al.* (2008) analysed a 7-yr-long ERT and borehole temperature monitoring data set at the Schilthorn, Swiss Alps and characterized both short-term (e.g. seasonal active layer dynamics) and long-term effects (e.g. ground ice degradation as a consequence of the extraordinary hot European summer in 2003). Dafflon *et al.* (2016) combined ERT with frequency-domain electromagnetic induction data, core analysis, and digital surface models to estimate

the spatial distribution of shallow permafrost in an Alaskan tundra environment. Oldenborger & LeBlanc (2018) imaged changes in unfrozen water content in accordance with temperature measurements alongside airport infrastructure.

While ERT is highly sensitive to unfrozen water content, quantitative estimates of ice from electrical data alone are impeded since ice and air are practically electrical insulators and may not be distinguished from a resistive rock matrix. Fortunately, air and ice usually differ by an order of magnitude in their acoustic velocities, in addition to velocity changes of up to 2000 m s^{-1} between frozen and unfrozen water (Hilbich 2010), making RST a valuable additional method in cryospheric geophysics (e.g. Harris & Cook 1986; Krautblatter & Draebing 2014; Steiner *et al.* 2019). For example, Dou & Ajo-Franklin (2014) performed seismic measurements in the arctic permafrost region and identified a low velocity zone, which is likely related to partially thawed saline permafrost and in agreement with ERT measurements by Hubbard *et al.* (2013). Merz *et al.* (2016) used ERT and RST measurements together with other geophysical as well as geotechnical data for a multidisciplinary characterization of an Alpine rock glacier. The authors combined the insights obtained from the different methods in a qualitative interpretation and concluded that joint inversions of different geophysical data sets offer opportunities for the quantification of permafrost composition in future studies.

To take advantage of the complementary sensitivities of ERT and RST for the quantification of permafrost constituents, Hauck *et al.* (2011) presented a petrophysical four-phase model (4PM) incorporating estimates of liquid water, ice and air contents for given separate inversions of electrical and seismic refraction data sets and a pre-existing porosity estimate. Mewes *et al.* (2017) assessed the resolution capacity of the 4PM, which depends on the individual resolution capacities of ERT and RST, with regard to the estimation of liquid water and ice contents for typical processes in the context of permafrost degradation. The authors emphasized that artifacts in the individual inversions can impair the physical plausibility of the estimated constituents and potentially lead to misinterpretation. They further found that smoothness regularization applied to the individual inversions can underestimate the magnitude of changes. Pellet *et al.* (2016) improved the 4PM through soil moisture calibration. Instead of prescribing the porosity, the authors developed an estimate of its distribution based on a three-phase model in the unfrozen part of the subsurface. They found that one remaining challenge in the application of the 4PM is the possibility of simulated ice occurrence even in regions where it is highly unlikely, highlighting the need for means to impose physical constraints during inversion. To this end, we present an approach that uses apparent resistivities and seismic traveltimes simultaneously in a petrophysically coupled joint inversion to improve the quantification of permafrost constituents from geophysical observations.

2 THEORY AND METHOD

2.1 Acoustic and electrical properties of partially frozen ground

Following Hauck *et al.* (2011), it is assumed that permafrost systems comprise the volumetric fractions of the solid rock matrix (f_r) and a pore-filling mixture of liquid water (f_w), ice (f_i) and air (f_a)

$$f_r + f_w + f_i + f_a = 1. \quad (1)$$

The volumetric fractions of the solid rock matrix, liquid water, frozen water and gaseous water or air, are herein referred to as rock, water, ice and air content, respectively. This terminology is chosen for the sole reason of brevity noting that both ice and air can represent different physical states of water, whereas the term rock is commonly used for the bulk medium. We emphasize that treatment of the rock content as a single phase is a simplification particularly favorable for Alpine permafrost, where the fraction of hard rock is much higher compared to shallow arctic permafrost for example. The latter may exhibit a pronounced and potentially clay-rich soil layer with very different acoustic and electrical properties than competent porous materials at larger depths.

The seismic slowness (s) of the four-phase system, that is, the reciprocal of the seismic P -wave velocity (v), is described by a time-averaging equation that sums up the slownesses of the individual components weighted by their respective volumetric fractions (e.g. Timur 1968)

$$s = \frac{1}{v} = \frac{f_w}{v_w} + \frac{f_i}{v_i} + \frac{f_a}{v_a} + \frac{f_r}{v_r}. \quad (2)$$

Eq. (2) assumes that the medium is isotropic, has a single homogeneous mineralogy, and is at high effective pressure (e.g. Mavko *et al.* 2009). References to alternative approaches better suited for the characterization of permafrost in unconsolidated materials are provided in the discussion.

Under the assumption that electrolytic conduction dominates, a modification of Archie's second law (Archie 1942) is used to describe the electrical resistivity of the bulk medium. As in Hauck *et al.* (2011), the porosity ϕ in the original form of Archie's second law is expressed in terms of the rock content, that is, $\phi = 1 - f_r$, while the liquid water saturation is replaced by the ratio of water content and porosity:

$$\rho = \rho_w (1 - f_r)^{-m} \left(\frac{f_w}{1 - f_r} \right)^{-n}. \quad (3)$$

Assuming prior estimates of porosity, the Archie parameters (cementation exponent m and saturation exponent n), pore water resistivity ρ_w , and the velocities of the four constituents, Hauck *et al.* (2011) used eqs (1), (2) and (3) to derive expressions for water, ice and air contents. These are then used to transform tomograms of ρ and s , obtained through individual inversions of ERT and RST data sets, into estimates of liquid water, ice, and air (Fig. 1a). The obtained estimates and their physical plausibility depend on the two tomograms and cannot be constrained directly. In the following, we describe a petrophysically coupled joint inversion approach, which uses both data sets to directly estimate the constituents of the four-phase system (Fig. 1b).

2.2 Petrophysical joint inversion for permafrost constituents

The parameter vector \mathbf{p} consists of the volumetric fractions of water, ice, air and rock for each model cell

$$\mathbf{p} = [f_w, f_i, f_a, f_r]^T. \quad (4)$$

Theoretically one could only invert for three phases and obtain the fourth one by subtraction from unity, but this would not safeguard against negative values in the fourth phase. Furthermore, having all four phases in the parameter vector enables flexible incorporation of prior information. During inversion, a transformed model vector \mathbf{m} is used, where each entry in \mathbf{p} is constrained to vary between zero and one by making use of logarithmic barriers such that

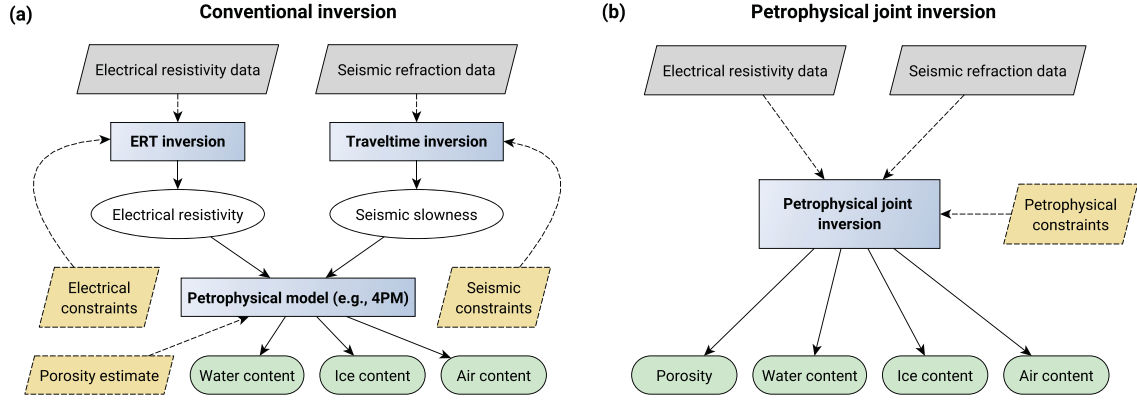


Figure 1. Schematic on the estimation of water, ice and air from ERT and RST data. (a) Conventional inversion of both data sets with subsequent petrophysical transformation. (b) Petrophysical joint inversion honoring both data sets and petrophysical relations during parameter estimation.

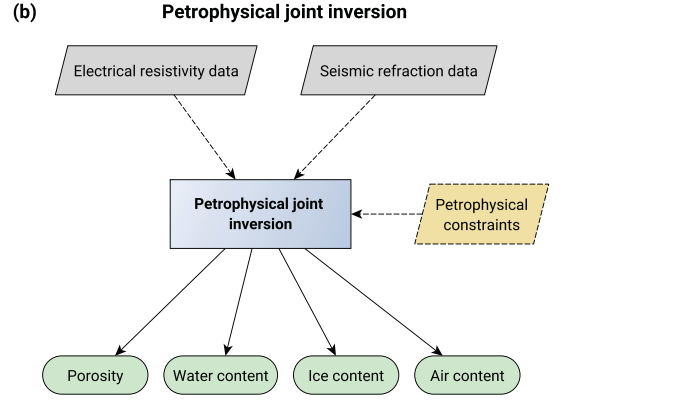
$m_j^k = \log(p_j^k) - \log(1 - p_j^k)$ after Kim & Kim (2011). The use of logarithmic barriers keeps each volumetric fraction within physical limits (i.e. $0 \leq f_w, f_i, f_a, f_r \leq 1$) while simultaneously reducing the ill-posedness of the inverse problem. Here, the indices j and k refer to spatial model cells and type of volumetric pore fraction, respectively. Traveltimes and logarithmized apparent resistivities are concatenated in the data vector

$$\mathbf{d} = [t, \log(\rho_a)]^T. \quad (5)$$

We minimize the following objective function:

$$\begin{aligned} & \|W_d(\mathbf{d} - \mathcal{F}(\mathbf{m}))\|_2^2 + \alpha^2 \|W_m \mathbf{m}\|_2^2 \\ & + \beta^2 \|W_p^{\text{sum}} \mathbf{p} - \mathbf{1}\|_2^2 \\ & + \gamma^2 \|W_p(\mathbf{p} - \mathbf{p}_0)\|_2^2 \rightarrow \min. \end{aligned} \quad (6)$$

The first term quantifies the misfit between observed data \mathbf{d} and the model response $\mathcal{F}(\mathbf{m})$ incorporating the reciprocals of the individual data errors on the diagonal of data weighting matrix W_d . Note that the model response $\mathcal{F}(\mathbf{m})$ contains petrophysical transformation according to eqs (2) and (3) followed by independent solutions of the RST and ERT forward problems. The second term represents a smoothness regularization applied to the model vector \mathbf{m} , where W_m is a block matrix holding four first-order roughness operators on its diagonal to promote smoothness in the distribution of each constituent of the four-phase system. The third term is an additional regularization term to fulfill the volume conservation constraint in eq. (1). Here, W_p^{sum} is a block matrix of four adjacent identity matrices acting on the untransformed petrophysical parameter vector \mathbf{p} to penalize solutions for which the sum of the four volumetric fractions deviates from unity. The fourth term represents a damping regularization and allows to incorporate *a priori* information on the petrophysical target parameters by penalizing deviations from a given reference model \mathbf{p}_0 . Here, W_p is a square matrix with either zeros or ones along its diagonal depending on which model parameters are sought to stay close to the reference model \mathbf{p}_0 . The fourth term is optional. For example, we discuss joint inversion results with and without a prescribed porosity distribution throughout this paper. The former uses $\gamma = 0$, whereas the latter uses $\gamma = \beta$ and $W_p = \text{diag}([\mathbf{0}, \mathbf{0}, \mathbf{0}, \mathbf{I}])$ to penalize solutions for which the rock content distribution deviates from its prior estimate. The dimensionless factors α and β scale the influence of the regularization terms. β is chosen large enough to prohibit non-physical solutions, while α is chosen to fit the data within error bounds.



To minimize the objective function (eq. 6), the following augmented system of normal equations is solved for the model parameter update $\Delta \mathbf{m}$ in a least-squares sense using the LSQR algorithm by Paige & Saunders (1982):

$$\begin{bmatrix} W_d \hat{J} \\ \alpha W_m \\ \beta \hat{W}_p^{\text{sum}} \\ \gamma \hat{W}_p \end{bmatrix} \Delta \mathbf{m} = \begin{bmatrix} W_d(\mathbf{d} - \mathcal{F}(\mathbf{m})) \\ -\alpha W_m \mathbf{m} \\ \beta(\mathbf{1} - \hat{W}_p^{\text{sum}} \mathbf{m}) \\ \gamma(\mathbf{p}_0 - \hat{W}_p \mathbf{m}) \end{bmatrix}. \quad (7)$$

Due to the use of logarithmic barriers, the transformed parameters \mathbf{m} are non-linear functions of the petrophysical target parameters \mathbf{p} . Since the volume conservation and damping constraints are acting on the latter, the model weighting matrices W_p^{sum} and W_p have to be scaled with the reciprocals of the partial derivative of \mathbf{m} with respect to \mathbf{p} at each iteration before multiplication with the model update $\Delta \mathbf{m}$, that is $\hat{W}_p = W_p \text{diag}(\partial \mathbf{m} / \partial \mathbf{p})^{-1}$ and $\hat{W}_p^{\text{sum}} = W_p^{\text{sum}} \text{diag}(\partial \mathbf{m} / \partial \mathbf{p})^{-1}$. Similarly, the Jacobian matrix \hat{J} is recomputed at each iteration $\hat{J} = J \text{diag}(\partial \mathbf{m} / \partial \mathbf{p})^{-1}$, where J holds the changes in traveltime and logarithmic apparent resistivity with respect to changes in the petrophysical target parameters:

$$J = \begin{bmatrix} \frac{\partial t}{\partial f_w} & \frac{\partial t}{\partial f_i} & \frac{\partial t}{\partial f_a} & \frac{\partial t}{\partial f_r} \\ \frac{\partial \log(\rho_a)}{\partial f_w} & \frac{\partial \log(\rho_a)}{\partial f_i} & \frac{\partial \log(\rho_a)}{\partial f_a} & \frac{\partial \log(\rho_a)}{\partial f_r} \end{bmatrix}. \quad (8)$$

The individual matrix entries are obtained by appropriate scaling of the common Jacobian entries of both methods. Scaling factors are dependent on the underlying petrophysical model (here eq. 2 and eq. 3) and detailed in Appendix A.

3 SYNTHETIC EXAMPLES

3.1 Synthetic model and data

To evaluate the performance of the joint inversion approach, a three-layer model is considered (Fig. 2a). Parameters are defined in terms of water, ice, air and rock contents and subsequently transformed into velocity and resistivity distributions for the generation of synthetic data. The model represents a typical layered scenario encountered in Alpine periglacial environments comprising a 5-m-thick, unfrozen active layer (i.e. the seasonal thaw layer), a 10-m-thick partially thawed layer with laterally changing ice and liquid water

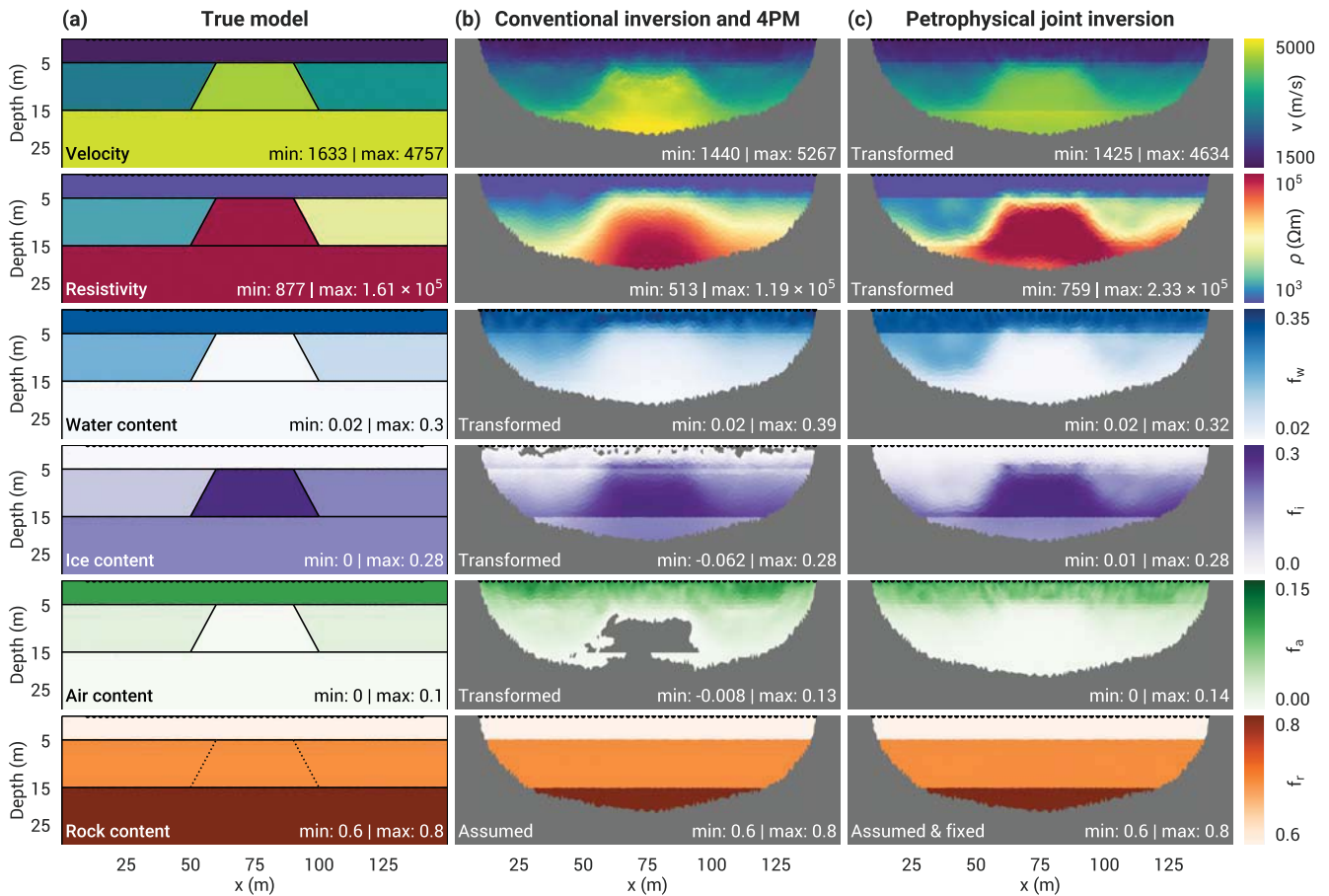


Figure 2. (a) True model, (b) conventional inversion results and (c) joint inversion results with *a priori* knowledge of the porosity distribution. All models are cut off below the lowermost ray path and in regions where the respective volumetric fraction is negative. Sensors are marked as black semicircles. Note that the electrical resistivity (second row) is displayed on a logarithmic colour scale. If not otherwise indicated in the lower left of each panel, the distributions shown in (b) and (c) directly result from the respective inversions. The annotation *Transformed* means that the respective quantity is obtained through transformation of the actual inversion results using petrophysical equations.

Table 1. Petrophysical parameters used in eq. (3) (left) and constituent velocities used in eq. (2) (right) for the synthetic examples. All parameters are assumed to be spatially constant.

Archie parameters			Constituent velocities		
Parameter	Value	Unit	Parameter	Value	Unit
ρ_w	150	Ωm	v_w	1500	m s^{-1}
n	2	–	v_i	3500	m s^{-1}
m	1.3	–	v_a	330	m s^{-1}
			v_r	5500	m s^{-1}

contents, and a frozen bedrock underneath. The porosity is decreasing from 40 to 20 per cent layer-wise with depth. Velocity and electrical resistivity are calculated according to eqs (2) and (3) with the parameters listed in Table 1 and generally increase with depth due to the decreases in liquid water and air contents, combined with increases in ice and rock contents.

While the acoustic velocities of water, ice, and air are agreed upon in the literature, v_r is strongly dependent on the type of rock (or soil). The chosen value of 5500 m s^{-1} may represent a metamorphic rock such as a pyritic paragneiss (e.g. Draebing & Krautblatter 2012). Common literature values are used for the Archie parameters (m and n), whereas the pore water resistivity ρ_w was chosen on the basis of laboratory measurements in an Alpine permafrost context (e.g.

Hauck & Kneisel 2008). All parameters in Table 1 are chosen to be constant throughout the model domain and not estimated during inversion. We refer to Hauck *et al.* (2011) for a sensitivity analysis of v_r , ρ_w , m and n in the context of ice estimation.

Synthetic traveltimes data are generated assuming 53 geophones spaced by 2.5 m and collocated shot positions resulting in 2756 shot-receiver pairs. Ray tracing utilizes the shortest path method with three additional nodes on each edge of a triangular model cell to increase the ray path accuracy following the approach outlined by Giroux & Larouche (2013). Traveltimes noise was added as additive Gaussian white noise (AGWN) with a standard deviation of 0.5 ms.

Electrode positions coincide with geophone locations. A dipole–dipole data set with dipole lengths of one, two and four unit electrode spacings is simulated neglecting absolute geometric factors above 5000 m resulting in 1414 apparent resistivities. Forward modelling employs quadratic shape functions, an enlarged forward modelling domain to avoid boundary effects, and is detailed by Rücker *et al.* (2006). A normally distributed relative error of 5 per cent was added to the simulated apparent resistivities. All conventional and joint inversion results presented in the following use four times larger smoothing in the horizontal direction to promote the expected layered structure and describe the synthetic data sets within their respective error bounds.

3.2 Inversion with correct porosity estimate

Conventional inversion results of traveltimes and apparent resistivities (Fig. 2b) are obtained using a Gauss–Newton scheme with smoothness regularization as detailed in Rucker *et al.* (2017). Velocity and electrical resistivity tomograms are transformed into distributions of water, ice and air using the 4PM and assuming that the porosity structure is known.

The different volumetric fractions are qualitatively and quantitatively in good agreement with the true model. Solely in the conductive and low velocity top layer, where the individual inversions exhibit small-scale variability close to the sensors, the 4PM produces small regions of negative ice content down to –6 per cent and overestimates the water content by up to 9 per cent.

Fig. 2(c) shows the results obtained with the developed petrophysical joint inversion approach. The quantitative agreement to the true model (Fig. 2a) is slightly better in comparison to the conventional inversion and the layer boundaries are more pronounced. Moreover, non-physical values do not occur close to the sensors.

3.3 Inversion with incorrect porosity estimate

We evaluate the inversion performance without detailed knowledge of the porosity distribution, as common for field applications (Fig. 3). Note that the true model has not changed, that is Figs 2(a) and 3(a) show identical distributions. For the conventional inversion, a homogeneous rock matrix content of 70 per cent (i.e. $\phi = 0.3$) is assumed (lowermost panel in Fig. 3b). This estimate is correct for the middle layer, but under- and overestimates the porosities of the top and bottom layer by 10 per cent, respectively, leading to non-physical ice content estimations in the top layer (reaching –14 per cent). In turn, ice contents in the bottom layer are strongly overestimated. This overestimation stems from the assumption of homogeneous porosity, as the high velocity below 15 m depth can no longer be explained by a porosity decrease and is compensated by additional ice. Furthermore, the air content in this region is non-physical (i.e. slightly below zero).

In the corresponding joint inversions, homogeneous rock content was only used as the starting model for f_r and allowed to vary by ± 15 per cent during the inversion. Estimates of water, ice and air contents are significantly improved through the joint inversion approach and do not exhibit any non-physical values (Fig. 3c). Moreover, the inversion indicates a porosity decrease with depth revealing that the measured data cannot be explained with the homogeneous starting model of f_r . The high ice content in the centre of the model cannot be reconstructed and is compensated by an increase in rock content.

3.4 Model parameter interdependency

To quantify the interdependency of water, ice, air and rock content, we consider the model covariance matrix of the coupled inverse problem. The model covariance elucidates how errors in the data are propagated into errors of the estimated model parameters. Diagonal elements represent variances of the corresponding parameters, while off-diagonal values indicate correlations between pairs of model parameters (e.g. Aster *et al.* 2012). For better illustration, the parameters are grouped into five discrete blocks as outlined in Fig. 3(a).

To highlight the need for petrophysical constraints, we compare the covariances of the coupled inverse problem without (Fig. 4a) and with volume conservation constraints (Fig. 4b). In the unconstrained

covariance matrix, the air content has the lowest diagonal values, partly due to generally small air contents in the model. In addition, the velocity of air differs significantly from the other constituent velocities (Table 1) leading to its generally good discriminability. For the remaining fractions, strong off-diagonal elements appear particularly in regions where the amount of unfrozen water is relatively high (parameters i, ii and iv). In comparison, the covariances are considerably lower in regions where the water content is low and no air exists (parameters iii and v). Covariances within one parameter group and between parameter groups are drastically reduced after applying volume conservation constraints in eq. (1) (Fig. 4b). Significant variances remain in the upper unfrozen part of the model (parameter i), where sensitivities are generally higher, indicating that errors in the data are more strongly reflected in errors in the model. In addition, strong variances are visible between ice and rock contents for the other parameters, that is, at greater depth.

4 FIELD DATA EXAMPLE

To demonstrate the applicability of the developed joint inversion approach to a real permafrost scenario, we consider a data set acquired at the Schilthorn site located in the Bernese Alps in Switzerland. The lithology of the Schilthorn massif mainly consists of ferruginous sandstone schists (Imhof *et al.* 2000). The bedrock weathering produced a fine-grained surface debris layer with a thickness up to 5 m (Hilbich *et al.* 2008). As part of the PACE project, a drilling campaign and first RST and ERT measurements were performed in 1998 to assess the presence of permafrost (Vonder Mühll *et al.* 2000). Borehole temperature measurements revealed warm permafrost, that is, near subzero temperature, where the liquid water content can be relatively high. The Schilthorn site became a reference monitoring site of PERMOS (Swiss Permafrost Monitoring Network, PERMOS 2016) including numerous measurements of temperature in three boreholes, ground surface temperature, soil moisture, ERT, RST, snow thickness, wind speed and direction, as well as solar radiation.

An ERT monitoring profile was initiated in 1999, automatized in 2009, extended in 2012 and is still maintained and functional (for data acquisition and preprocessing details see Hilbich *et al.* 2008, 2011; Mollaret *et al.* 2018). The ERT acquisition system is composed of 49 fixed electrodes spaced by 2 m connected to a GeoTom device (GEOLOG, Germany) used with a Wenner configuration. We only consider the first half of this permanent profile, where collocated geophone positions exist to ensure equal lateral coverage of both methods. The seismic signal is generated by a sledge hammer striking a steel plate at 25 shot positions located in between each geophone and recorded through a Geode device (Geometrics, USA). First breaks were manually picked and seismic traveltime errors were estimated to range between 0.1 and 0.5 ms (Hilbich 2010). We use 0.3 ms as an error estimate for the RST data and 3 per cent relative error for the ERT data. Similarly as for the inversion of synthetic data, all conventional and joint inversion results use four times larger smoothing in the horizontal direction to promote layered subsurface structures.

We consider a data set measured on 19 August 2014 presented by Pellet *et al.* (2016). On that day, the thaw layer depth in the two boreholes available along the profile was observed around 2.1 m depth. In warm recent years, maximum thaw depths at the end of summer reached 9–10 m indicative of considerable permafrost degradation (PERMOS 2019). Fig. 5(a) shows the conventional inversion results with a subsequent application of the 4PM using

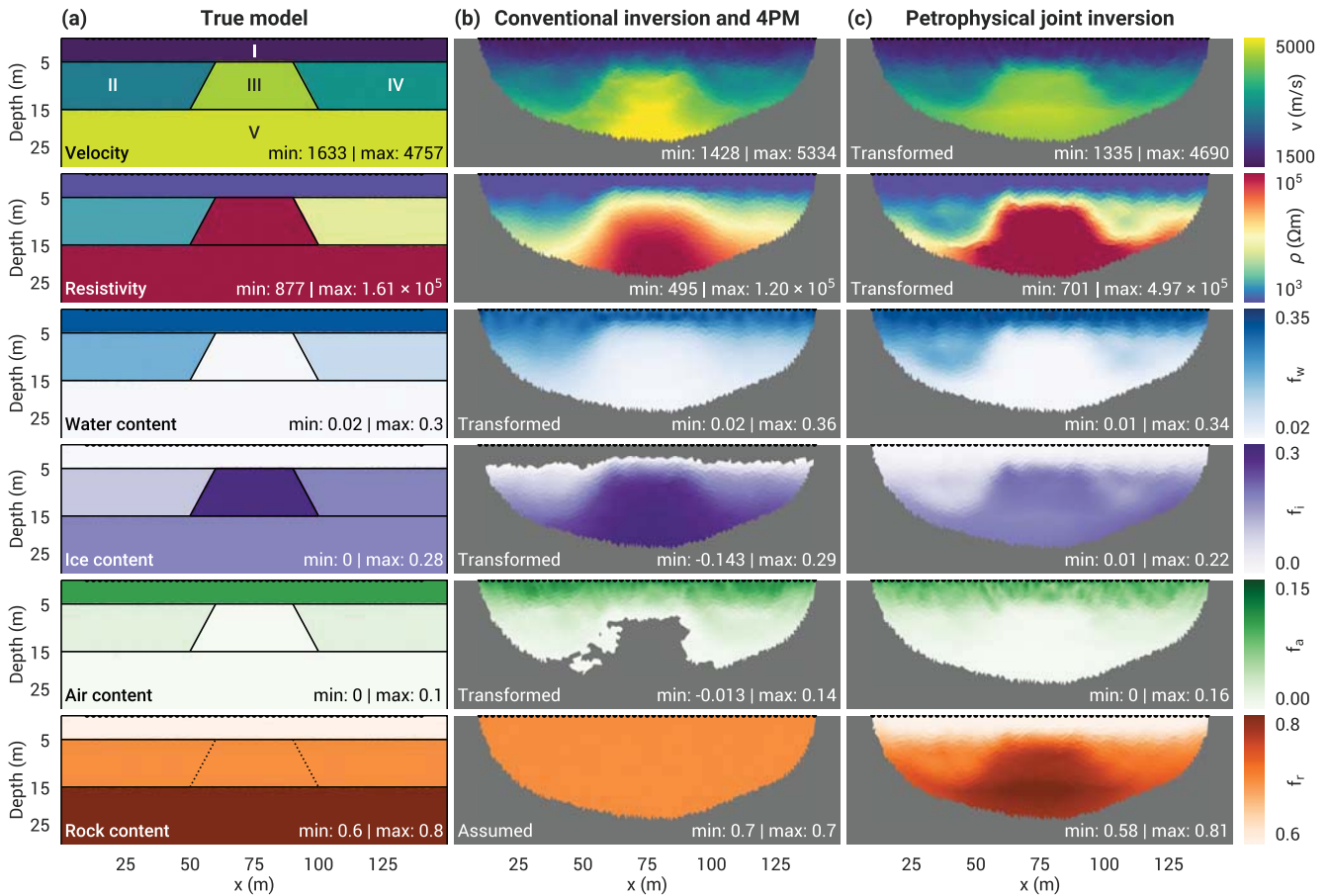


Figure 3. As Fig. 2 but without *a priori* knowledge of the porosity distribution.

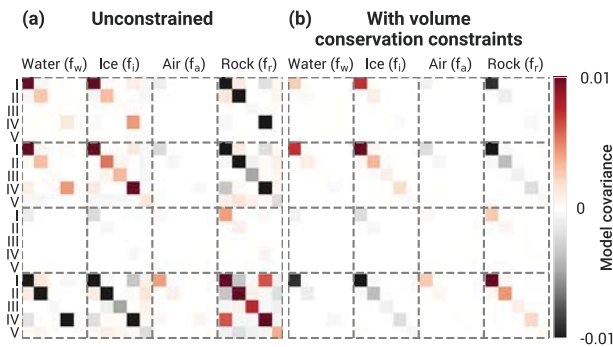


Figure 4. Model covariance matrix for the petrophysical joint inversion. Red and black indicate strong positive and negative parameter covariance, white indicates no correlation. The Roman numbering of the model parameters is depicted in Fig. 3(a).

the parameters from Pellet *et al.* (2016) as listed in Table 2 and a constant porosity of 53 per cent based on *in situ* measurements performed by (Scherler 2006). To allow comparability with previous Schilthorn studies (e.g. Hilbich *et al.* 2008; Pellet *et al.* 2016), water, ice and air contents are displayed as saturations, that is divided by porosity.

With a prescribed and constant porosity, the conventional approach can only satisfy the low velocities near the surface with non-physical values for ice and air saturations reaching -142 and $+207$ per cent, respectively (Fig. 5a). In contrast, non-physical

values do not occur in the petrophysical joint inversion results, as lower porosities near the surface (Fig. 5b) are allowed during parameter estimation.

Since the joint inversion is formulated in terms of the petrophysical target parameters, it becomes possible to include prior information, for example, constraints on water content based on soil moisture measurements or temperature-dependent constraints on ice occurrence. Here, we demonstrate the latter by constraining ice contents to zero, where the measured borehole temperatures (shown in Figs 6a and 7a) are positive. This is achieved by creating a box with a radius of 2 m around the corresponding depth interval of the borehole (as indicated for ice saturation in Fig. 5c) and adding cells in this box to the damping constraint in eq. (6). To allow for sharp transitions in the vertical direction across the known thaw depth, we disable smoothing regularization across the lower boundary of this box (by setting the corresponding entries of W_m to zero). A similar approach has been used by Wunderlich *et al.* (2018) to constrain ERT inversion results to direct push electrical conductivity logs.

While generally comparable to the unconstrained version (Fig. 5b), no ice appears in the upper 2 m around the boreholes in the joint inversion result with borehole constraints (Fig. 5c). The decrease in ice also affects deeper parts of the model and is compensated by an increase in rock content (i.e. a decrease in porosity), which in turn leads to higher water saturations. The air saturation in all three approaches is high in the thawed part of the model and quickly approaches zero at larger depths.

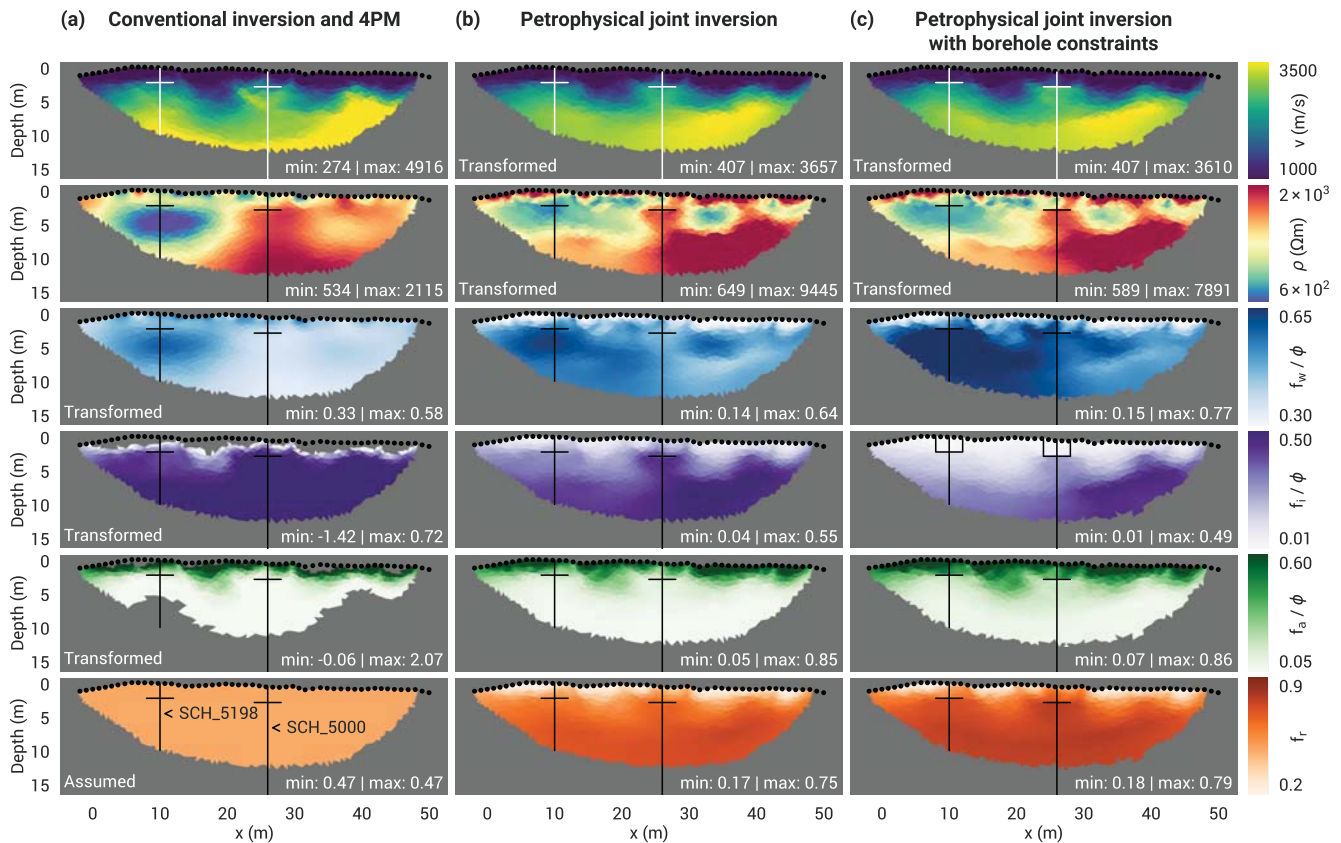


Figure 5. Tomograms of the Schilthorn field data sets obtained through (a) conventional inversion, (b) joint inversion and (c) joint inversion with borehole constraints. If not otherwise indicated in the lower left of each panel, the shown distributions directly result from the respective inversions. All models are cut off below the lowermost ray path and in regions where the respective saturation is negative or exceeds one. Sensors are marked as black circles. Note that the electrical resistivity (second row) is displayed on a logarithmic colour scale. Boreholes and associated thaw depths are marked as vertical and horizontal lines, respectively. The black boxes superimposed on the ice saturation in (c) mark the regions where the ice content has been constrained to zero.

Table 2. Petrophysical parameters used in eq. (3) (left) and constituent velocities used in eq. (2) (right) for the field data example taken from Pellet et al. (2016). All parameters are assumed to be spatially constant.

Archie parameters			Constituent velocities		
Parameter	Value	Unit	Parameter	Value	Unit
ρ_w	60	Ωm	v_w	1500	m s^{-1}
n	2.4	–	v_i	3500	m s^{-1}
m	1.4	–	v_a	300	m s^{-1}
			v_r	6000	m s^{-1}

To highlight quantitative differences between the different inversion approaches, Figs 6 and 7 show the measured borehole temperatures with depth together with the inversion results shown in Fig. 5 extracted at the borehole locations. The effect of logarithmic barriers can be seen in Fig. 6(c) for instance, where in contrast to the conventional approach, joint inversion results do not cross the zero line.

While the conventional inversion and joint inversion without borehole constraints show smooth transitions of ice saturation in the upper few meters for example, the added borehole constraints result in sharp transitions, that is, a better delineation of the thawed layer (e.g. Fig. 7c). Again, it can be seen how the decrease in ice (e.g. Fig. 7c) is causing an increase in rock content (e.g. Fig. 7e), which in turn increases water saturation (e.g. Fig. 7b).

5 DISCUSSION

Transformation of conventionally inverted velocity and resistivity tomograms into estimates of water, ice and air can lead to non-physical results in the presence of data errors and incorrect porosity estimates. For the Schilthorn case, this was also found by Pellet et al. (2016), who then derived porosity in the unfrozen part from a three-phase model calibrated to shallow soil moisture measurements and assumed a gradient porosity in the deeper part. With the assumption of porosity decrease with depth and soil moisture measurements, Pellet et al. (2016) obtained tomograms comparable to our results from the petrophysical joint inversion, which used no prior information on porosity.

Petrophysical joint inversion combines the information of RST and ERT measurements and leads to quantitatively improved images by honoring petrophysical relations and volume conservation during parameter estimation. Inversion of synthetic data without a porosity estimate (Fig. 3c) and analysis of the model covariances has revealed a strong ambiguity between ice and rock contents. This ambiguity also became apparent in the application to field data and is in agreement with the findings by Hauck et al. (2011). The authors analytically explored the range of possible values for ice, water, air, and rock contents for a given pair of resistivity and velocity values. By comparing the spread of solutions, it was found that air and water content can be discriminated quite well even if porosity is unknown, while there is a strong ambiguity between ice and rock contents.

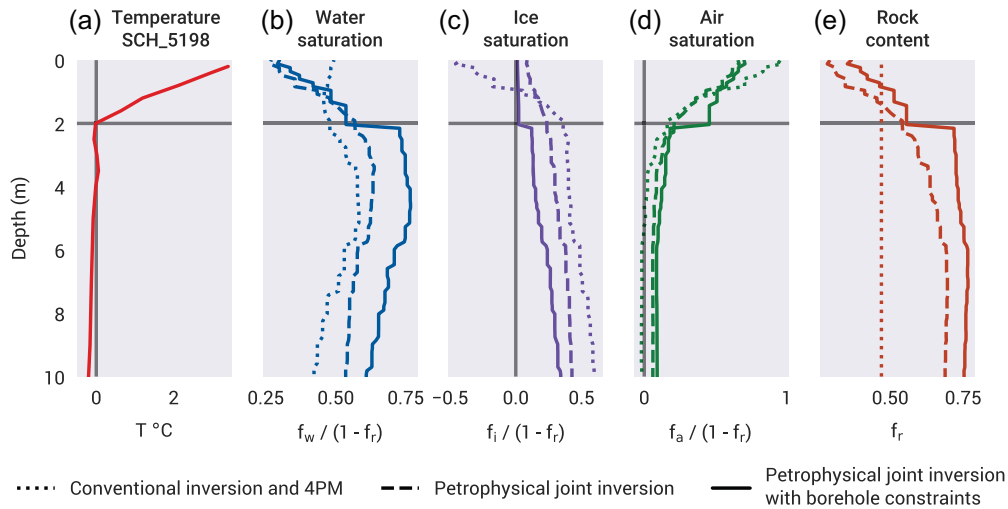


Figure 6. (a) Temperature measured on 19 August 2014 in borehole SCH_5198 and (b–e) corresponding four-phase constituents derived from conventional inversion and petrophysical joint inversion without and with borehole constraints. The horizontal and vertical grey lines mark the thaw depth and zero line, respectively. The borehole location is depicted in the lower left panel of Fig. 5.

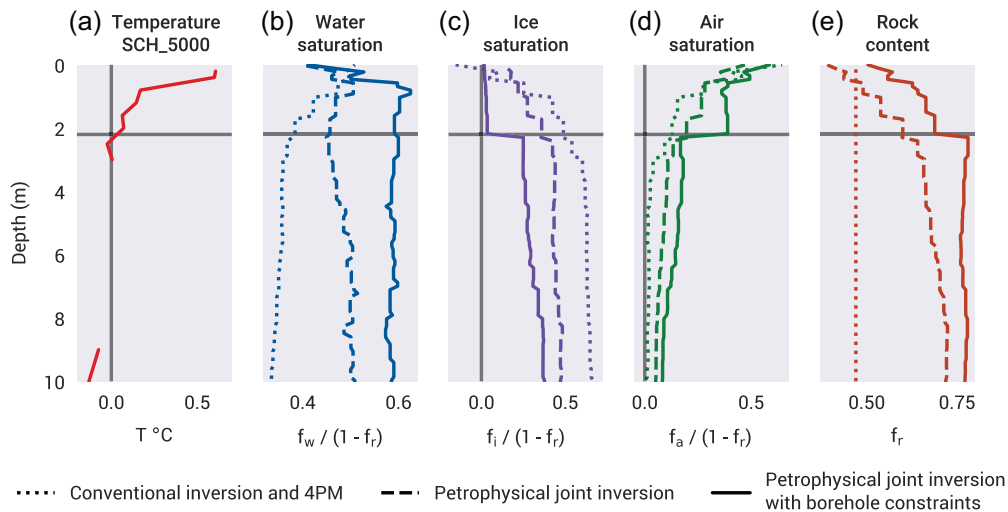


Figure 7. (a) Temperature measured on 19 August 2014 in borehole SCH_5000 and (b–e) corresponding four-phase constituents derived from conventional inversion and petrophysical joint inversion without and with borehole constraints. The horizontal and vertical grey lines mark the thaw depth and zero line, respectively. The borehole location is depicted in the lower left panel of Fig. 5.

The discriminability between ice and rock matrix could be improved by incorporation of additional freeze–thaw sensitive data sets such as complex electrical resistivity measurements. Results of first laboratory (Wu *et al.* 2013; Kemna *et al.* 2014) and field studies (Grimm & Stillman 2015; Mudler *et al.* 2019) hold promise for ice quantification, as the spectral response of frozen ground is strongly affected by the electrical polarization characteristics of ice. Ambiguity could further be reduced in a monitoring context, where the porosity can be assumed to be constant within the observed period (Hauck *et al.* 2017). Inclusion of multiple timesteps into a time-lapse joint inversion therefore represents a promising extension to this work.

The approach presented is not restricted to the empirical model by Archie (1942) and the time-averaging equation by Timur (1968) and does not attempt to address their general shortcomings. For example, a general and often overlooked problem is that the empirical factors (e.g. the saturation exponent) are commonly assumed to

be spatially constant in field applications. Future extensions of our work could incorporate advanced petrophysical formulations more representative for the studied field sites.

For the case of saline permafrost for example, Wu *et al.* (2017) presented a modified formulation, which takes structural soil changes as well as temperature-dependent salinity changes (i.e. electrical conductivity changes) of unfrozen water during freeze–thaw transitions into account. Based on a field survey on a rock glacier and associated laboratory measurements, Duvillard *et al.* (2018) emphasized that surface conduction can be significant and has to be taken into account when estimating liquid water content in environments where electrolytic conduction is not dominating the bulk electrical conductivity. For the case of low-porosity hard rocks, Draebing & Krautblatter (2012) presented a modified Timur equation that accounts for changes in matrix velocity due to ice pressure. Dou *et al.* (2017) presented a two-end-member mixing approach accounting for the coexistence of frame-strengthening and

pore-filling ice to describe the *P*-wave velocity in saturated, unconsolidated saline permafrost, where conventional slowness averaging would be inadequate.

6 CONCLUSIONS

We have developed a petrophysical joint inversion approach that uses seismic traveltimes and apparent resistivities to image distributions of water, ice, air and rock content. Since petrophysical relations and volume conservation are honored during parameter estimation, our approach produces physically meaningful results, even in the absence of correct porosity estimates, and thereby outperforms post-inversion transformation of conventional tomograms. A significant advantage is that the inversion constraints can be formulated in terms of the petrophysical target parameters facilitating the flexible use of *a priori* information and direct incorporation of non-geophysical data, for example, constraints on water content inferred from soil moisture measurements, into the inversion.

An application to a field data set from the Schilthorn, Swiss Alps, has revealed physically plausible tomograms in agreement with previous studies without relying on suitable *a priori* porosity estimates. We conclude that our method contributes to improved quantification of water, ice and air from geophysical observations and will therefore be of direct use for researchers and practitioners in cryogeophysical and hydrogeophysical applications.

Yet joint inversion alone is not able to overcome the inherent petrophysical ambiguities between ice and rock matrix, which remain to be addressed in future studies through additional (non-)geophysical observations, advanced petrophysical formulations and monitoring applications. To facilitate adoption and further development of the method, we made the algorithm available under a permissive BSD license. It is based on the open-source modeling and inversion library *pyGIMLi* (Rücker *et al.* 2017). The implementation as well as scripts to reproduce results and figures of this paper can be found at <https://github.com/florian-wagner/four-phase-inversion>.

ACKNOWLEDGEMENTS

The first author gratefully acknowledges funding received by the Dr. Erich Ritter foundation in cooperation with the Water Science Alliance, which allowed preparation of this paper during a research visit at Lawrence Berkeley National Laboratory inspired by many fruitful discussions with Baptiste Dafflon, Sebastian Uhlemann and other colleagues in the Earth and Environmental Sciences Area. The constructive comments by editor Jörg Renner, Adam Booth and three anonymous reviewers helped to improve earlier versions of this manuscript. We thank Carsten Rücker for his dedication to the development of *pyGIMLi*.

REFERENCES

- Archie, G., 1942. The electrical resistivity log as an aid in determining some reservoir characteristics, *Trans. AIME*, **146**, 54–62.
- Aster, R.C., Borchers, B. & Thurber, C.H., 2012. *Parameter Estimation and Inverse Problems*, 2nd edn, Academic Press.
- Dafflon, B., Hubbard, S., Ulrich, C., Peterson, J., Wu, Y., Wainwright, H. & Kneafsey, T.J., 2016. Geophysical estimation of shallow permafrost distribution and properties in an ice-wedge polygon-dominated arctic tundra region, *Geophysics*, **81**, WA247–WA263.
- Dou, S. & Ajo-Franklin, J.B., 2014. Full-wavefield inversion of surface waves for mapping embedded low-velocity zones in permafrost, *Geophysics*, **79**(6), EN107–EN124.
- Dou, S., Nakagawa, S., Dreger, D. & Ajo-Franklin, J., 2017. An effective-medium model for *P*-wave velocities of saturated, unconsolidated saline permafrost, *Geophysics*, **82**(3), EN33–EN50.
- Draebing, D. & Krautblatter, M., 2012. *P*-wave velocity changes in freezing hard low-porosity rocks: a laboratory-based time-average model, *Cryosphere*, **6**(5), 1163–1174.
- Duvillard, P.A., Revil, A., Qi, Y., Soueid Ahmed, A., Coperey, A. & Ravel, L., 2018. Three-dimensional electrical conductivity and induced polarization tomography of a rock glacier, *J. geophys. Res.: Solid Earth*, **123**(11), 9528–9554.
- Giroux, B. & Larouche, B., 2013. Task-parallel implementation of 3D shortest path raytracing for geophysical applications, *Comput. Geosci.*, **54**, 130–141.
- Grimm, R.E. & Stillman, D.E., 2015. Field test of detection and characterisation of subsurface ice using broadband spectral-induced polarisation, *Permafrost Periglacial Process.*, **26**(1), 28–38.
- Harris, C. & Cook, J.D., 1986. The detection of high altitude permafrost in Jotunheimen, Norway using seismic refraction techniques: an assessment, *Arctic Alpine Res.*, **18**(1), 19–26.
- Hauck, C. & Kneisel, C., 2008. *Applied Geophysics in Periglacial Environments*, Cambridge University Press.
- Hauck, C., Böttcher, M. & Maurer, H., 2011. A new model for estimating subsurface ice content based on combined electrical and seismic data sets, *Cryosphere*, **5**, 453–468.
- Hauck, C., Hilbich, C. & Mollaret, C., 2017. A time-lapse geophysical model for detecting changes in ground ice content based on electrical and seismic mixing rules, in *Proceedings of the 23rd European Meeting of Environmental and Engineering Geophysics*, EAGE Publications BV.
- Hilbich, C., 2010. Time-lapse refraction seismic tomography for the detection of ground ice degradation, *Cryosphere*, **4**(3), 243–259.
- Hilbich, C., Hauck, C., Hoelzle, M., Scherler, M., Schudel, L., Völsch, I., Vonder Mühl, D. & Mäusbacher, R., 2008. Monitoring mountain permafrost evolution using electrical resistivity tomography: a 7-year study of seasonal, annual, and long-term variations at Schilthorn, Swiss Alps, *J. geophys. Res.*, **113**(F1), doi:10.1029/2007JF000799.
- Hilbich, C., Fuss, C. & Hauck, C., 2011. Automated time-lapse ERT for improved process analysis and monitoring of frozen ground, *Permafrost Periglacial Process.*, **22**(4), 306–319.
- Hubbard, S.S. *et al.*, 2013. Quantifying and relating land-surface and subsurface variability in permafrost environments using LiDAR and surface geophysical datasets, *Hydrogeol. J.*, **21**(1), 149–169.
- Huggel, C., Clague, J.J. & Korup, O., 2012. Is climate change responsible for changing landslide activity in high mountains?, *Earth Surf. Process. Landforms*, **37**, 77–91.
- Imhof, M., Pierrehumbert, G., Haeberli, W. & Kienholz, H., 2000. Permafrost investigation in the schilthorn massif, bernese alps, switzerland, *Permafrost Periglacial.*, **11**(3), 189–206.
- Kemma, A., Weigand, M. & Zimmermann, E., 2014. Resistivity and SIP response of rocks during freezing and thawing, in *Proceedings of the 3rd International Workshop on Induced Polarization*, Oléron Island, France.
- Kim, H.J. & Kim, Y.H., 2011. A unified transformation function for lower and upper bounding constraints on model parameters in electrical and electromagnetic inversion, *J. Geophys. Eng.*, **8**, 21–26.
- Krautblatter, M. & Draebing, D., 2014. Pseudo 3-D *P* wave refraction seismic monitoring of permafrost in steep unstable bedrock, *J. geophys. Res.: Earth Surface*, **119**(2), 287–299.
- Mavko, G., Mukerji, T. & Dvorkin, J., 2009. *The Rock Physics Handbook - Tools for Seismic Analysis of Porous Media*, Cambridge University Press.
- Merz, K., Maurer, H., Rabenstein, L., Buchli, T., Springman, S.M. & Zweifel, M., 2016. Multidisciplinary geophysical investigations over an alpine rock glacier, *Geophysics*, **81**(1), WA147–WA157.
- Mewes, B., Hilbich, C., Delaloye, R. & Hauck, C., 2017. Resolution capacity of geophysical monitoring regarding permafrost degradation induced by hydrological processes, *Cryosphere*, **11**(6), 2957–2974.
- Mollaret, C., Hilbich, C., Pellet, C., Flores Orozco, A., Delaloye, R. & Hauck, C., 2018. Mountain permafrost degradation documented through a network of permanent electrical resistivity tomography sites, *Cryosphere Discuss.*, **1**, 1–34.

- Mudler, J., Hördt, A., Przyklenk, A., Fiandaca, G., Maurya, P.K. & Hauck, C., 2019. Two-dimensional inversion of wideband spectral data from the capacitively coupled resistivity method – first applications in periglacial environments, *Cryosphere Discuss.*, **2019**, 1–24.
- Oldenborger, G.A. & LeBlanc, A.-M., 2018. Monitoring changes in unfrozen water content with electrical resistivity surveys in cold continuous permafrost, *J. geophys. Int.*, **215**, 965–977.
- Paige, C.C. & Saunders, M.A., 1982. LSQR: An algorithm for sparse linear equations and sparse least squares, *ACM Trans. Math. Softw.*, **8**(1), 43–71.
- Pellet, C., Hilbich, C., Marmy, A. & Hauck, C., 2016. Soil moisture data for the validation of permafrost models using direct and indirect measurement approaches at three Alpine sites, *Front. Earth Sci.*, **3**, 91.
- PERMOS, 2016. Permafrost in Switzerland 2010/2011 to 2013/2014., Glaciological Report Permafrost No. 12-15 of the Cryospheric Commission of the Swiss Academy of Sciences, 85.
- PERMOS, 2019. Permafrost in Switzerland 2014/2015 to 2017/2018., Glaciological Report Permafrost No. 16-19 of the Cryospheric Commission of the Swiss Academy of Sciences, 104.
- Rücker, C., Günther, T. & Spitzer, K., 2006. Three-dimensional modelling and inversion of dc resistivity data incorporating topography – I. Modelling, *J. geophys. Int.*, **166**(2), 495–505.
- Rücker, C., Günther, T. & Wagner, F.M., 2017. pyGIMLi: an open-source library for modelling and inversion in geophysics, *Comput. Geosci.*, **109**, 106–123.
- Scherler, M., 2006. Messung und Modellierung konvektiver Wärmetransportprozesse in der Auftauschicht von Gebirgs-Permafrost am Beispiel des Schilthorns, *Master's thesis*, University of Zürich.
- Schuur, E.A.G. *et al.*, 2015. Climate change and the permafrost carbon feedback, *Nature*, **520**, 171–179.
- Steiner, M., Wagner, F.M. & Flores Orozco, A., 2019. Improved characterization of alpine permafrost through structurally constrained inversion of refraction seismic data, *Cryosphere Discuss.*, **2019**, 1–27.
- Timur, A., 1968. Velocity of compressional waves in porous media at permafrost temperatures, *Geophysics*, **33**, 584–595.
- Vonder Mühl, D.S., Hauck, C. & Lehmann, F., 2000. Verification of geophysical models in alpine permafrost using borehole information, *Ann. Glaciol.*, **31**, 300–306.

- Wu, Y., Hubbard, S.S., Ulrich, C. & Wulfschleger, S.D., 2013. Remote monitoring of freeze-thaw transitions in arctic soils using the complex resistivity method, *Vadose Zone J.*, **12**.
- Wu, Y., Nakagawa, S., Kneafsey, T.J., Dafflon, B. & Hubbard, S.S., 2017. Electrical and seismic response of saline permafrost soil during freeze-thaw transition, *J. appl. Geophys.*, **146**, 16–26.
- Wunderlich, T. *et al.*, 2018. Constraining electric resistivity tomography by direct push electric conductivity logs and vibracores: an exemplary study of the Fiume Morto silted riverbed (Ostia Antica, western Italy), *Geophysics*, **83**(3), B87–B103.

APPENDIX A: PETROPHYSICALLY TRANSFORMED JACOBIAN

Changes in travelttime and apparent resistivity with respect to changes in the petrophysical target parameters are obtained by chain rule splitting, where the outer derivative represents the common Jacobian entries of both methods, that is, $\partial t/\partial s$ and $\partial \log(\rho_a)/\partial \log(\rho)$, whereas the inner derivative applies appropriate petrophysical scaling according to eqs (2) and (3). Additional multiplication with ρ/ρ_a accounts for the logarithmic transform used in the Jacobian entries of the conventional geoelectrical inverse problem.

$$\begin{aligned}
 \mathbf{J} &= \begin{bmatrix} \frac{\partial t}{\partial \log(\rho_a)} & \frac{\partial t}{\partial \log(\rho_a)} & \frac{\partial t}{\partial \log(\rho_a)} & \frac{\partial t}{\partial \log(\rho_a)} \\ \frac{\partial f_w}{\partial \log(\rho_a)} & \frac{\partial f_i}{\partial \log(\rho_a)} & \frac{\partial f_a}{\partial \log(\rho_a)} & \frac{\partial f_r}{\partial \log(\rho_a)} \end{bmatrix} \\
 &= \begin{bmatrix} \frac{\partial t}{\partial s} \frac{\partial s}{\partial \rho_a} \frac{\partial \rho}{\partial \rho} & \frac{\partial t}{\partial s} \frac{\partial s}{\partial \rho_a} \frac{\partial \rho}{\partial \rho} & \frac{\partial t}{\partial s} \frac{\partial s}{\partial \rho_a} \frac{\partial \rho}{\partial \rho} & \frac{\partial t}{\partial s} \frac{\partial s}{\partial \rho_a} \frac{\partial \rho}{\partial \rho} \\ \frac{\partial f_w}{\partial \rho_a} \frac{\partial \rho}{\partial \rho} & \frac{\partial f_i}{\partial \rho_a} \frac{\partial \rho}{\partial \rho} & \frac{\partial f_a}{\partial \rho_a} \frac{\partial \rho}{\partial \rho} & \frac{\partial f_r}{\partial \rho_a} \frac{\partial \rho}{\partial \rho} \end{bmatrix} \\
 &= \begin{bmatrix} \frac{\partial t}{\partial s} \frac{1}{\rho_a} & \frac{\partial t}{\partial s} \frac{1}{\rho_a} & \frac{\partial t}{\partial s} \frac{1}{\rho_a} & \frac{\partial t}{\partial s} \frac{1}{\rho_a} \\ -\frac{\rho}{\rho_a} \frac{\partial \rho_a}{\partial \rho} \frac{n}{f_w} \rho & 0 & 0 & \frac{\rho}{\rho_a} \frac{\partial \rho_a}{\partial \rho} \left(\frac{m-n}{1-f_r} \right) \rho \end{bmatrix} \quad (\text{A1})
 \end{aligned}$$